

Article

In-Situ Photoelectron Spectroscopy Investigation of Sulfurization-Induced Sodiophilic Sites with Model Systems of α -sexithiophene and *p*-sexiphenyl

Yuan Liu ^{1,2} , Xu Lian ^{2,3}, Chonglai Jiang ^{1,2}, Zejun Sun ², Jinlin Yang ^{2,*}, Yishui Ding ^{1,2} and Wei Chen ^{1,2,4,*}

¹ Joint School of National University of Singapore and Tianjin University, International Campus of Tianjin University, Binhai New City, Fuzhou 350207, China

² Department of Chemistry, National University of Singapore, 3 Science Drive 3, Singapore 117543, Singapore

³ Centre for Advanced 2D Materials, National University of Singapore, 6 Science Drive 2, Singapore 117546, Singapore

⁴ Department of Physics, National University of Singapore, 2 Science Drive 3, Singapore 117542, Singapore

* Correspondence: yjlchem@nus.edu.sg (J.Y.); phycw@nus.edu.sg (W.C.); Tel.: +(65)-9866-8649 (J.Y.); +(65)-6516-2921 (W.C.)

Abstract: Uncontrollable sodium dendrite growth results in poor cycling performance and severe safety issues, hindering practical applications of sodium metal batteries (SMBs). To stabilize sodium metal anodes (SMAs), various strategies have been developed including employing anode hosts and electrolyte additives to establish protective layers. Nevertheless, the understanding of interaction mechanisms between protective materials and SMAs is still limited, which is crucial for the rational design of protective materials. In this work, we investigated the interaction mechanism between sodium metal and sulfur-containing functional groups with comparative model systems of α -sexithiophene (6T) and *p*-sexiphenyl (6P) through in-situ photoelectron spectroscopy investigations and density functional theory (DFT) calculations. Our results show that sodium atoms tend to interact with sulfur atoms and their connected carbon atoms simultaneously as well as the aromatic carbon atoms of the end groups of 6T molecules, while no chemical interaction between Na and 6P molecules is observed. The observed sulfurization-induced sodiophilic sites can shed light on the rational design of sulfur-containing protective materials and the relevant interface engineering to stabilize SMAs.

Keywords: SMAs; sulfurization; organic semiconductor; sodiophilic sites; in-situ XPS/UPS



Citation: Liu, Y.; Lian, X.; Jiang, C.; Sun, Z.; Yang, J.; Ding, Y.; Chen, W. In-Situ Photoelectron Spectroscopy Investigation of Sulfurization-Induced Sodiophilic Sites with Model Systems of α -sexithiophene and *p*-sexiphenyl. *Batteries* **2023**, *9*, 21. <https://doi.org/10.3390/batteries9010021>

Academic Editors: Yuanhua Xiao, Ling Wu, Xianwen Wu, Yiping Tang and Carlos Ziebert

Received: 21 November 2022

Revised: 22 December 2022

Accepted: 24 December 2022

Published: 27 December 2022



Copyright: © 2022 by the authors. Licensee MDPI, Basel, Switzerland. This article is an open access article distributed under the terms and conditions of the Creative Commons Attribution (CC BY) license (<https://creativecommons.org/licenses/by/4.0/>).

1. Introduction

In order to satisfy the increasing demand for high-energy storage systems, sodium metal batteries (SMBs) have recently been regarded as prospective candidates for next-generation high-energy rechargeable devices. Within the same alkali metal group, sodium metal anodes (SMAs) possess similar properties to lithium metal anodes (LMAs), e.g., low redox potential (-2.71 V vs standard hydrogen electrode) and high theoretical capacity (1166 mAh g^{-1}). Moreover, they are more favoured due to the low cost (US\$ 4 kg $^{-1}$) and high abundance of Na on earth (2.3% in the crust) [1,2]. Nevertheless, some challenges hinder the practical application of SMAs, including uncontrollable sodium dendrite growth, huge volume expansion, poor cycling performance, and severe safety issues [3,4]. Due to the high (electro)chemical reactivity of Na, SMAs can reduce most of the liquid organic electrolyte components spontaneously and induce the formation of a porous and organic-rich solid electrolyte interphase (SEI) on the anode surface. During cycling progress, the volume fluctuation of SMAs is nearly infinite due to their hostless nature, thus inducing cracks and continuous formation/deformation of SEI. Moreover, uncontrollable sodium dendrite growth also happens due to the inhomogeneous SEI, which can further penetrate through the separator and result in short circuits as well as severe safety issues for the batteries.

Strategies towards stabilizing SMAs in liquid electrolytes mainly include employing anode hosts, adjusting electrolyte compositions, and fabricating artificial protective layers. Employing anode hosts (carbon-, metal-, and composite-based frameworks) is a useful method to tolerate the huge volume change during cycling, and the large surface area of the host materials can effectively regulate the local current density [5,6]. Moreover, through heteroatom doping (e.g., OCF [7], NSCNT [8]), surface functionalization (e.g., h - Ti_3C_2 /CNTs [9]), and seed implantation (e.g., Sn@C [10], $Co_{SA}@NC$ [11]), the sodiophilicity of the anode hosts can be easily designed and improved, thus inducing a uniform and dense deposition of sodium [12]. Adjusting electrolyte compositions is a facile but effective method to generate robust and homogeneous SEI layers, including developing ether-based electrolytes (e.g., NaPF₆/glyme [13], NaBF₄/diglyme [14]), concentrated electrolytes (e.g., 4M NaFSI-DME [15], 2.1 M NaFSI/DME+BTfE [16]), ionic liquids (e.g., Na-Cl-IL [17], ether-[C₄C₁im][BF₄] [18]), and electrolyte additives (e.g., FEC [19], nitrofullerene [20], KTFSI [21]). An ideal SEI is beneficial for suppressing the volume expansion and dendrite growth, inducing uniform sodium deposition, stable cycling properties, and improved safety [22]. Since SEI layers are generated by the reaction between sodium anodes and electrolyte components, adjusting electrolyte compositions can directly change the compositions of SEI layers, thus improving their properties. Fabricating an artificial protective layer before battery assembly is another effective way to build an ideal SEI since the protective materials can be rationally designed without the effect of the electrochemical process. The protective passivation layers can impede direct contact between SMAs and electrolytes and prevent the in-situ formation of porous and inhomogeneous SEIs, thus regulating sodium deposition, suppressing dendrite growth, and limiting volume change [1,23]. In view of this, diverse effective artificial SEI layers have been developed, including organic (e.g., PVDF [24], PhS₂Na₂ [25]), inorganic (e.g., sodium halides [26,27], Na₃P [28], Al₂O₃ [29]), and hybrid (e.g., PVDF-NaF [30], Al₂O₃-PVdF-HFP [31]) layers.

Although recent studies have achieved great performance improvement for SMBs using the abovementioned strategies, most of them are result-oriented and only focus on the performance of batteries, paying less attention to the exploration of the specific mechanisms. Moreover, the protective materials studied in SMAs are usually imitated from those in LMAs, which may have less or even reverse effects, due to the different properties between alkali metals. For instance, compared to lithium metal, sodium metal has higher reactivity with a larger atomic radius (Na: 1.86 Å; Li: 1.52 Å), thus interacting with electrolyte components more violently and making it harder to form a uniform and stable SEI [2,3]. In addition, sodium metal possesses a relatively lower mechanical strength (bulk modulus - Na: 6.3 GPa; Li: 11 GPa), making it easier to form “dead” sodium, but suppressing sodium dendrite growth by a robust SEI is also more effective [2,3]. Based on these differences, it is reported that the imitated electrolyte additive (Na₂S₆-NaNO₃) has an adverse effect in SMAs, in contrast to the prior findings in the LMAs [32,33]. Consequently, in order to rationally design novel protective materials for SMAs, it is necessary to develop a deeper understanding of the interaction mechanisms between SMAs and protective materials.

Thiophene derivative materials have been widely studied in various batteries, including use as anode hosts [34], separators [35], and electrolyte additives [36] in lithium metal batteries (LMBs), and use as anode materials in metal ion batteries [37,38]. To explore their application in SMBs, understanding the interaction process between Na metal and the sulfur-containing functional groups is of great importance. In this work, we conducted an in-situ photoelectron spectroscopy investigation of the interaction process between sodium metal and protective materials, using α -sexithiophene (6T) and p -sexiphenyl (6P) molecules as model systems. With these simplified model systems, the interaction process between sodium metal and sulfur-containing functional groups was investigated without the effects of complex battery systems. The sulfurization-induced interaction process is unravelled. Induced by the sulfur-containing functional groups, at 6T/Na interface, Na atoms prefer to interact with the sulfur atoms and their connected carbon atoms as well as the aromatic carbon atoms of the terminal groups. Comparatively, at 6P/Na interface,

no chemical interaction process happens, but a strong charge transfer process is observed with band bending effect and formation of LUMO-derived state. Our study sheds light on the sulfurization-induced sodiophilic sites through in-situ investigation of model systems, which can provide insights into the rational design of novel sulfur-containing protective materials for SMAs.

2. Materials and Methods

In-situ photoelectron spectroscopy investigations were carried out using a customer-designed ultra-high vacuum (UHV) system [39]. Two deposition processes were studied: (1) Na metal was deposited on organic (6T or 6P) molecules to simulate the interaction process between Na and anode hosts; (2) organic (6T or 6P) molecules were deposited on Na films to simulate the interaction process between electrolyte additives and SMAs. Silicon and tungsten substrates were used for each process, respectively, having been thoroughly degassed through resistive heating at 500 °C. Sodium metal was deposited using an alkali metal dispenser (SAES Getters) with a 4.00 A current applied. Vacuum sublimation purified organic molecules (Tokyo Chemical Industry) were deposited using a resistively heated single Knudsen cell evaporator at 175 °C for 6T and 225 °C for 6P. After each deposition process in the preparation chamber, the sample was transferred to the analysis chamber directly for in-situ photoelectron spectroscopy characterizations. These two chambers are connected under UHV conditions: the preparation chamber has a pressure below 2×10^{-8} mbar, and the analysis chamber has a pressure below 3×10^{-10} mbar. In-situ X-ray/ultraviolet photoelectron spectroscopy (XPS/UPS) experiments were conducted at room temperature with the Al K α (1486.7 eV) X-ray source (Omicron DAR400) and He I (21.2 eV) UV source (Fermi BL1010s), and the excited photoelectrons were detected by the hemispherical analyzer (Omicron EA125) (resolution: 0.05 eV). To measure the work function, a -10 V bias voltage was applied to samples to obtain the secondary electron cut-off (SECO). CasaXPS software was used for core-level spectra decomposition using a Shirley background and a GL(50) line shape (50% Gaussian plus 50% Lorentzian function). The deposition thickness is estimated based on the intensities of XPS core-level peaks and inelastic mean free path (IMFP) formulas [40].

To characterize the thickness and surface morphology, atomic force microscopy (AFM) characterizations were conducted using the BRUKER Dimension Fast Scan AFM system for the pre-deposited organic films on silicon substrates. Sodium wettability tests were conducted by soaking Cu and 6T/6P-coating Cu foils into the molten sodium pool (150 °C) for 1 min and then comparing the amount of attached sodium metal on samples. Moreover, the molten sodium was dropped on the samples to compare their contact angles. To further study the favorable sodiophilic sites, density functional theory (DFT) calculations were also conducted using Gaussian 16 software with a B3LYP-D3BJ/6-311G(d,p) level of theory [41,42]. The adsorption energy was calculated as the energy difference between the molecule and the sum of a molecule and a Na atom.

3. Results and Discussion

In order to study the sulfurization-induced sodiophilic sites, 6T and 6P were selected as the model molecules. They have similar linear structures with π -conjugated systems and can be easily grown on various substrates under UHV conditions. Compared to 6P, 6T molecules have unique sulfur-containing functional groups. Through this comparative model study, a deeper understanding of the interaction process between sulfur-containing organic materials and SMAs can be achieved. Our proposed mechanisms and key results are shown in Figure 1. When Na atoms are deposited on 6T molecules, the molecules are standing on silicon substrates, similar to the situation in previous reports [43,44]; thus, Na atoms can diffuse into them and interact with both sides of molecules, inducing more reduced carbon species (Figure 1a). For the reverse deposition order, when 6T molecules are deposited on Na films, molecules are lying down similarly to deposition on Ag [45–47] and Au [48] metal, and different interaction sites are observed (Figure 1a). To further study

and verify the interaction process induced by sulfurization, 6P molecules were studied as a comparison. It is found that no chemical interaction happens for either deposition sequence, but a strong charge transfer is detected for both Na deposition on 6P and 6P deposition on Na (Figure 1b). Our results confirm that the interaction process between 6T and Na is induced by the sulfurization of molecules, and the favorable sodiophilic sites are discussed below in detail with the help of in-situ photoelectron spectroscopies and DFT calculations. Based on these sulfurization-induced sodiophilic sites, the improved sodiophilicity of Cu current collector was verified through sodium wettability tests (Figure S1). After soaking Cu foils and coated Cu foils in the molten sodium pool, the 6T-coated Cu foil has the most attached sodium on its surface.

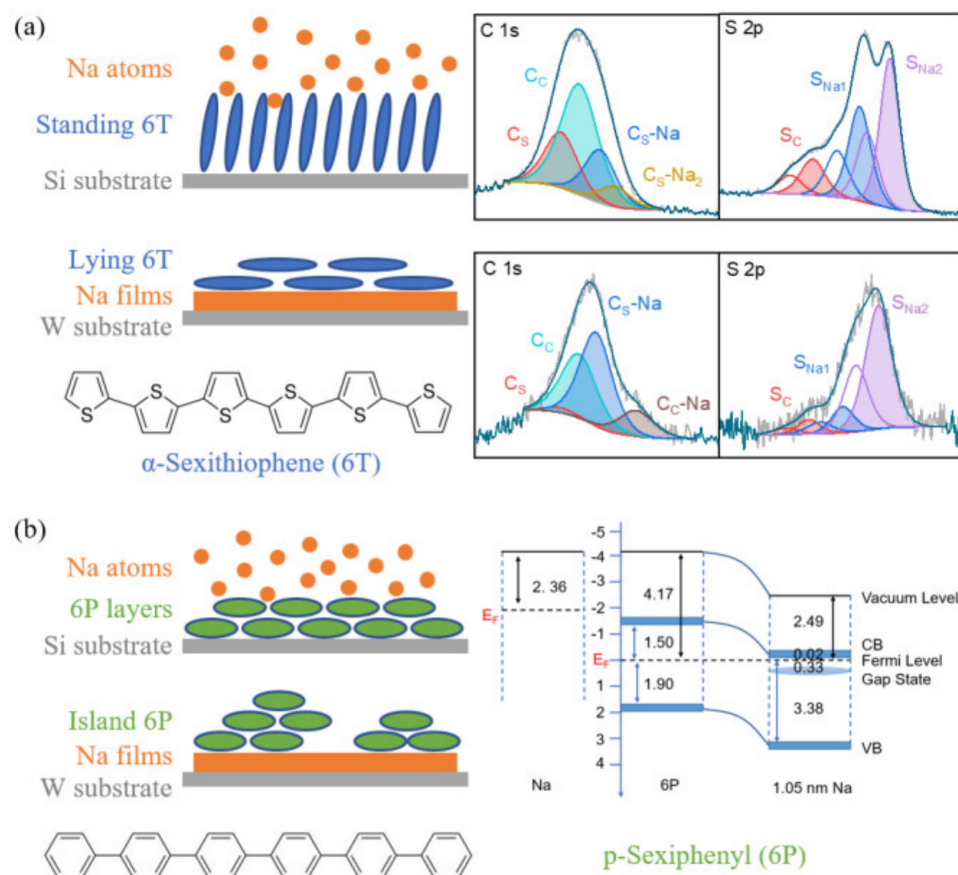


Figure 1. (a) Proposed mechanism of Na interaction with 6T molecules with different deposition orders and the XPS spectra indicating the interaction sites. (b) Proposed mechanism of Na interaction with 6P molecules with different deposition orders and the band bending effect at the 6P/Na interface.

3.1. Na-6T

3.1.1. Na on 6T

To simulate the interaction process between host materials and sodium metal, 6T molecules were first deposited on silicon substrates, and then Na atoms were deposited stepwise on molecule films for in-situ XPS/UPS experiments (Figure 2a). As shown in Figure 2b, for pristine 6T molecules [49–51], the C 1s peak contains two different components: one is connected to sulfur atoms with a higher binding energy at 285.5 eV (shown as C_S); the other is connected only to carbon atoms with a lower binding energy at 284.8 eV (shown as C_C). In S 2p region, the spin-orbit doublet peaks are observed with an area ratio of 2:1, which originate from the same sulfur species (shown as S_C) located at 164.5 eV for $2p_{3/2}$ and 165.7 eV for $2p_{1/2}$. For UPS spectra, the work function of 6T molecules is measured as 2.85 eV and smaller than the previously reported value, which is related to the molecule orientation and the deposition thickness on silicon substrates [43]. As shown in

Figure S2, with increasing standing 6T deposited, the work function gradually decreases to 1.47 eV or even lower. Since the thickness of 6T films was characterized as 19.1 nm through AFM characterization (Figure S3), it is reasonable for the films to have a work function of 2.85 eV. Moreover, for the pristine 6T molecules, the highest occupied molecular orbital (HOMO) onset is at 1.80 eV below the Fermi level, and the valence band shape is consistent with the reported one, indicating the successful preparation of 6T layers [52–54].

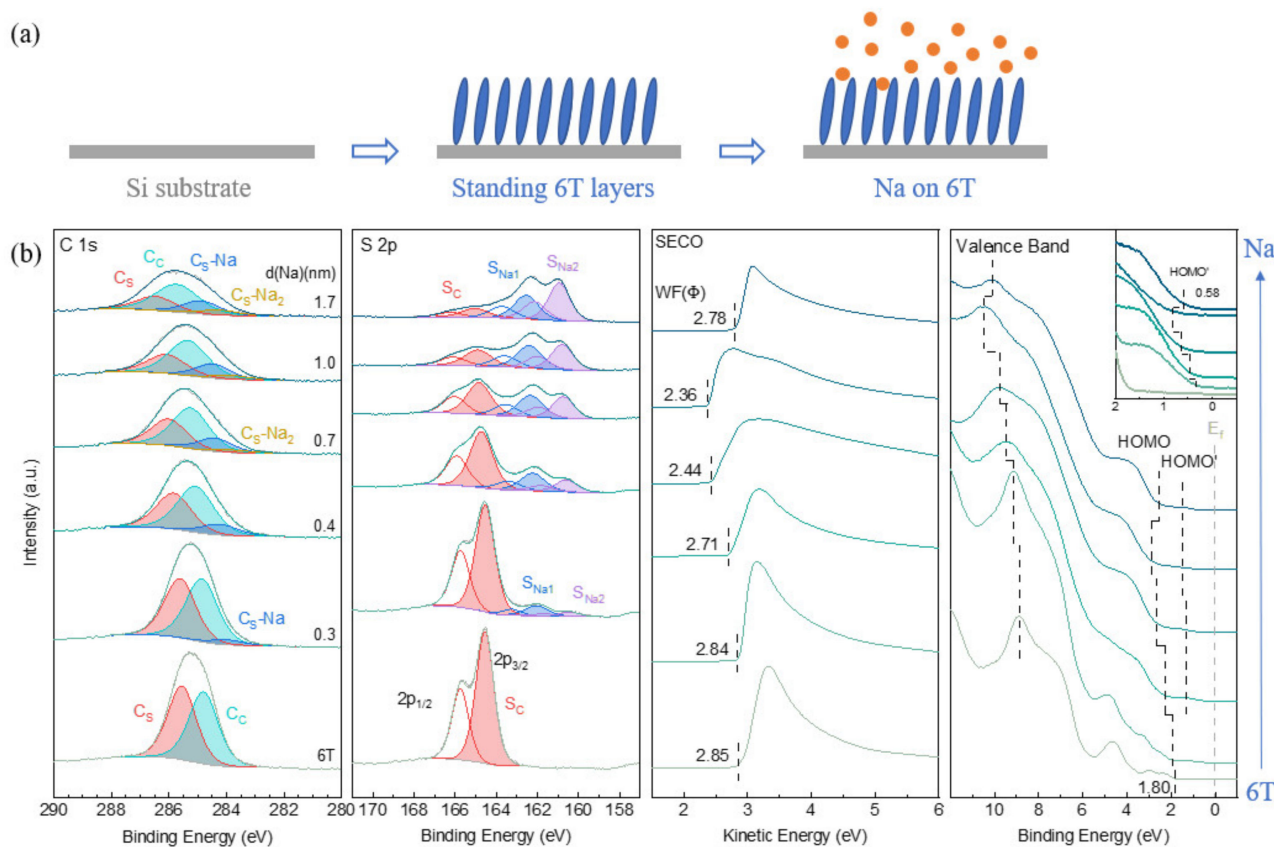


Figure 2. (a) Schematic of the 6T molecules and Na atoms deposition sequences. (b) XPS and UPS spectra of 6T films with stepwise Na deposition on a silicon substrate.

After the preparation of 6T films, Na atoms were deposited stepwise to study the interaction process at 6T/Na interface (Figure 2b). With 0.3 nm Na deposited, two reduced sulfur species (shown as S_{Na1} and S_{Na2}) are detected, which are located at 2.5 eV and 4.1 eV lower binding energy (relative to S_C), respectively, indicating the reduction of S_C atoms by Na metal. Meanwhile, the relevant reduced carbon species (shown as C_{S-Na}) is also observed at 1.6 eV lower binding energy (relative to C_S), while the C_C signal remains unchanged. These reduced species indicate the first-step interaction between Na and 6T molecules: S atoms and their connected C_S atoms are reduced by Na metal, and one S atom can be reduced by two Na atoms simultaneously. With thicker Na deposited, the signals of reduced sulfur and carbon species become stronger, and one more reduced carbon species (shown as C_{S-Na₂}) is observed at 0.7 nm Na deposition, which is located at 2.2 eV lower binding energy (relative to C_S). Additionally, as shown in Figure S4, the Na 1s peak has the same full width at half maximum (FWHM) during the deposition process, indicating no new oxidized Na species is formed in this second interaction step. Therefore, for this step, we propose that the interaction sites between Na and 6T are the same as those in the first step, which is related to the 6T deposition mode. On silicon substrates, 6T molecules are deposited in standing mode, thus enabling Na atoms to diffuse into molecules and interact on both sides of them at the same sites. In this way, the reduced C_S atoms can be further reduced on the other side, resulting in the generation of C_{S-Na₂} species. In general, for the

interaction process at the 6T/Na interface, Na atoms interact with sulfur atoms and their connected carbon atoms first and then interact with the same sites of 6T molecules on the other side.

In-situ UPS experiments were also conducted to study the electronic structure evolution during the interaction process (Figure 2b). With Na deposition, the work function of 6T molecules gradually decreases due to the reacted Na-6T formation and charge transfer from Na to 6T. In addition, in the valence band region, it is detected that the typical signals of pristine 6T molecules gradually weaken and broaden with the interaction process. Moreover, a new HOMO state is observed with the onset at 0.58 eV at 1.7 nm Na deposition, which originates from the reacted Na-6T caused by the charge transfer from Na to the unoccupied state of 6T. The huge electronic structure change of 6T molecules shows clear evidence of the strong interaction between 6T and Na.

3.1.2. 6T on Na

The reverse deposition order was further studied to simulate the interaction between SMAs and electrolyte additives, in which 6T molecules were stepwise deposited on Na films for in-situ XPS/UPS characterizations (Figure 3a). According to Figure S4, when 6T molecules are deposited on Na films, the Na 1s peak shows a higher FWHM compared to that for Na on 6T, indicating more oxidized Na species. Thus, we propose different interaction sites and deposition modes of 6T molecules for this reverse deposition sequence. With thin 6T molecules deposited on Na films, nearly all sulfur signals originate from the two reduced sulfur species (shown as S_{Na1} and S_{Na2}), and two reduced carbon species (shown as C_S -Na and C_C -Na) are observed. The reduced S_{Na1} and S_{Na2} species are located at 1.8 eV and 3.7 eV lower binding energy (relative to S_C), and the reduced C_S -Na and C_C -Na species are located at 1.5 eV and 2.3 eV lower binding energy (relative to C_S and C_C , respectively). Similarly, the reduced S_{Na1} , S_{Na2} , and C_S -Na species indicate the interaction between Na atoms and S_C atoms as well as their connected C_S atoms. It should be noted that the binding energies of reduced S_{Na1} and S_{Na2} atoms relative to S_C atoms are higher with this reverse deposition sequence, which is related to the different molecule deposition modes. 6T molecules deposited on Na films are lying down, thus Na atoms can hardly diffuse into them. In this way, strong interaction and charge transfer only happen at the interface, inducing the smaller binding energy difference between S_C atoms of pristine 6T molecules and S_{Na1}/S_{Na2} atoms of reduced Na-6T molecules. Moreover, it is also observed that S_{Na1} and S_{Na2} signals gradually weaken with increasing 6T deposition without any transformation between S_{Na1} and S_{Na2} species, which also verifies that the interaction only happens at the interface. For the reduced C_C -Na species in the C 1s region, this indicates a new interaction site caused by the different molecule deposition mode. Since 6T molecules are lying down, and there is nearly no diffusion of Na into 6T, the interaction between 6T and Na can only happen on one side of molecules. In this case, we propose that C_C atoms can also be reduced by the excess Na atoms, generating the reduced C_C -Na species. In general, for the Na/6T interface, Na can interact with sulfur atoms and their connected carbon atoms as well as the aromatic carbon atoms.

The electronic structure evolution was also studied through in-situ UPS experiments (Figure 3b). Similarly, with increasing molecule deposited, the work function of films gradually increases, and the valence band shape of Na gradually transfers to that of pristine 6T molecules since the reacted Na-6T are covered below the pristine 6T molecules. Compared to Na deposited on 6T films, no new HOMO state is detected in this reverse deposition sequence since the interaction only happens at the interface. The detection thickness of UPS is too surficial to detect the new weak signal formed below the bulk pristine 6T. Thus, the in-situ UPS results can also verify that the interaction only happens at the Na/6T interface.

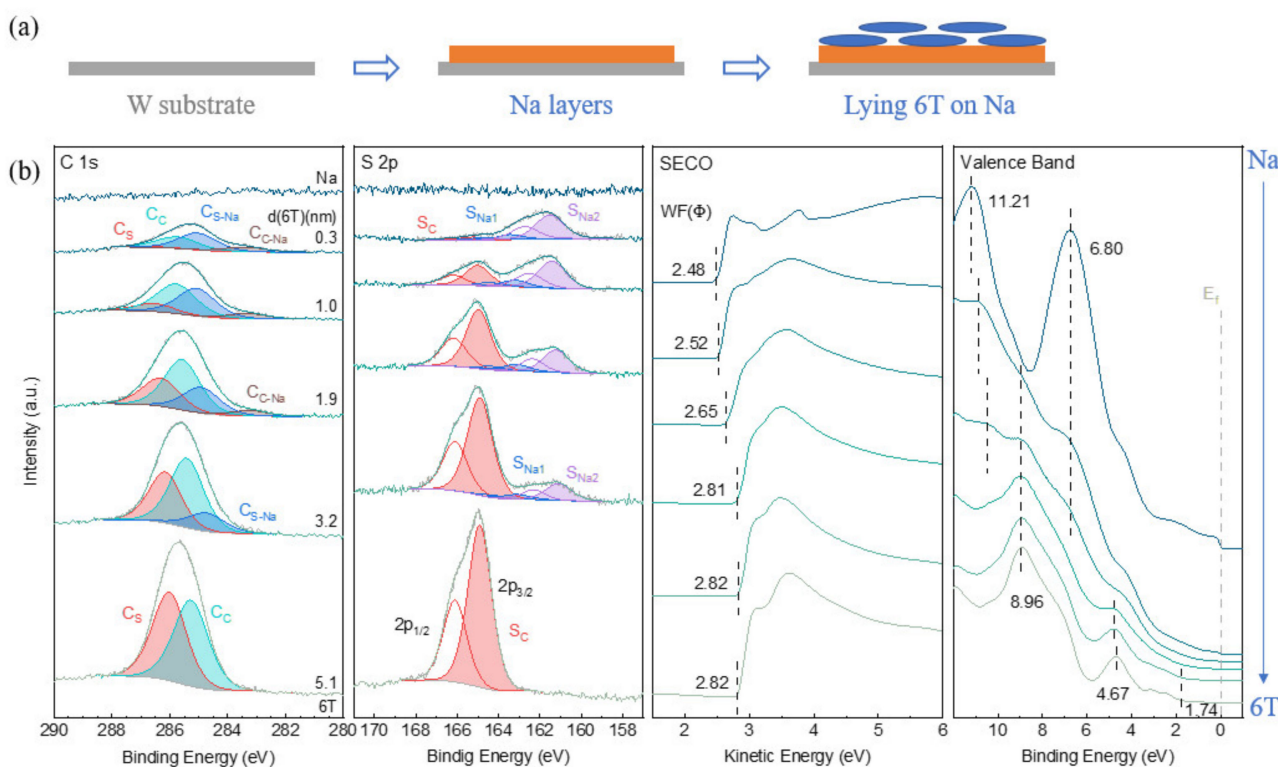


Figure 3. (a) Schematic of the 6T molecules and Na atoms deposition sequences. (b) XPS and UPS spectra of Na films with stepwise 6T deposition on a tungsten substrate.

3.2. Na-6P

3.2.1. Na on 6P

To further demonstrate the effect of sulfurization on the sodiophilic sites, the interaction process between 6P and Na was studied for comparison. Na was firstly stepwise deposited on 6P films to simulate the interaction between the anode host materials and the deposited Na (Figure 4a). For pristine 6P films, the thickness was measured as 20.2 nm through AFM (Figure S3), and the XPS/UPS characterization results (Figure 4b) are in good agreement with previous reports [55–57]. There is only one kind of atom: aromatic carbon atoms located at 284.6 eV. The work function of the 6P layers is measured as 4.16 eV, and the HOMO onset is located at 1.90 eV. After Na deposition, it is found that the carbon peak shape remains symmetric with only slight broadening during the deposition process. Moreover, the valence band shape also remains the same as that of the pristine 6P molecules and unchanged during the Na deposition. It indicates that no chemical reaction happens between Na and 6P molecules. However, strong charge transfer from Na to 6P molecules is observed. As shown in C 1s region, the carbon peak gradually shifts to the higher binding energy side with Na deposited. Meanwhile, the work function of the sample gradually decreases, and the valence band peaks show similar shifts to the higher binding energy side. This is due to the band bending effect of 6P molecules caused by the charge transfer [58]. Since the work function of 6P molecules is larger than that of Na metal, when they are in contact, charge transfer happens from Na metal to 6P molecules to make the Fermi level aligned. However, because of the lack of free charge carriers in the organic semiconductors, the electrons will accumulate at the interface, inducing a space charge region with the electric field. Under the electric field, the energy band edges are continuously shifted, and the bands are bent downward towards the interface, shown as the higher binding energy of the occupied levels. The strong charge transfer is also verified by the formation of the new state with the onset located at 0.33 eV as shown in the HOMO edge region. With charge transfer from Na atoms to 6P molecules, the lowest unoccupied molecular orbital (LUMO) state of 6P is occupied and can be detected as the new HOMO state near the Fermi level,

which is also reported in previous articles about 6P/Cs [55], 6P/K [59], and 6P/Ca [60]. Therefore, for the 6P/Na interface, no chemical reaction happens, but strong charge transfer is observed with the band bending effect.

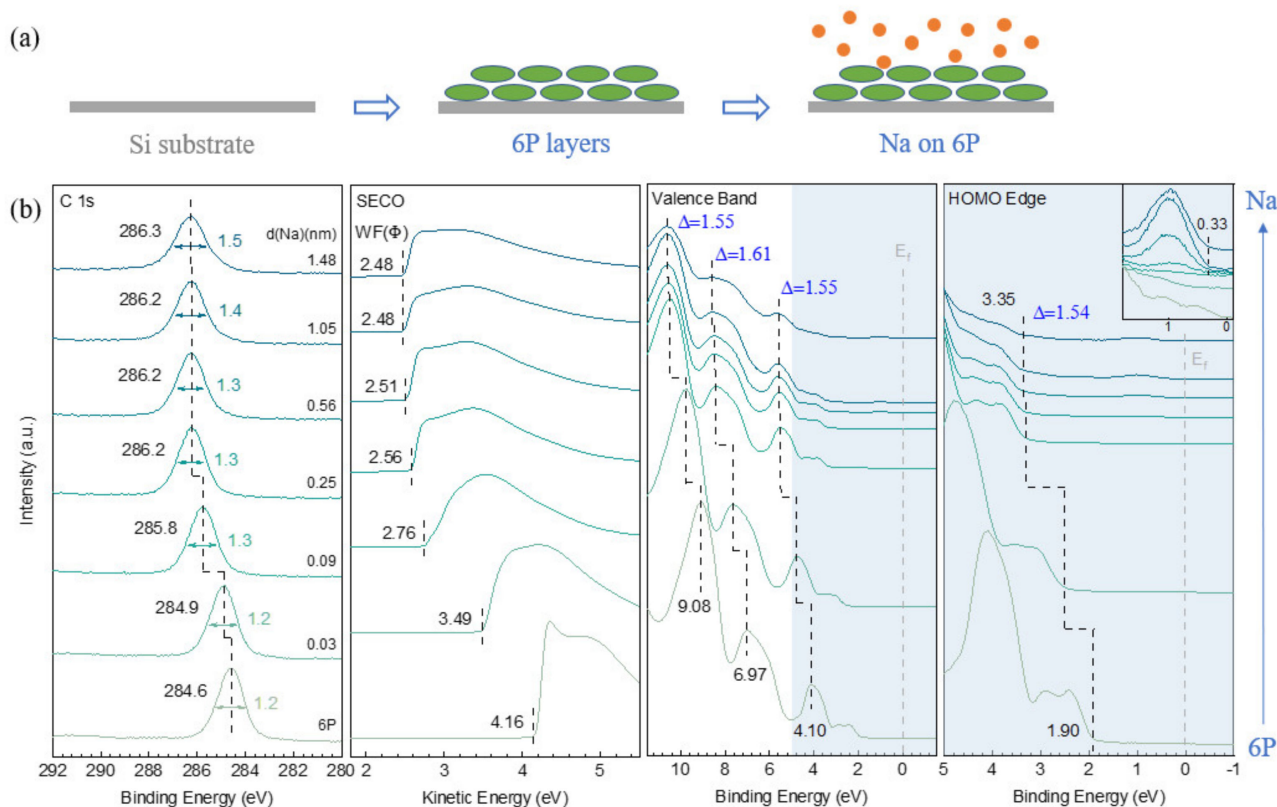


Figure 4. (a) Schematic of the 6P molecules and Na atoms deposition sequences. (b) XPS and UPS spectra of 6P films with stepwise Na deposition on a silicon substrate.

3.2.2. 6P on Na

The reverse deposition sequence was also studied to simulate the interaction between SMAs and electrolyte additives (Figure 5a). Similar to the 6P/Na interface, no chemical reaction is detected, and a strong charge transfer is observed. As shown in Figure 5b, with 6P molecules deposited on Na films, the valence band shape transfers to that of pristine 6P molecules and remains unchanged, indicating that no chemical reaction happens. However, it is noticed that the C 1s peak shape is asymmetric which is different from that of pristine 6P molecules when the deposition thickness is thinner than 2.7 nm. This is due to the stacking mode of 6P [61,62]. When there is only a small amount of 6P deposited, they are grown via island mode, thus inducing different binding energies of C 1s and the asymmetric peak. With more 6P molecules deposited, they are reorganized and shown as having a regular deposition mode, inducing the more symmetric C 1s peak with a deposition thickness thicker than 5.2 nm. In addition, the strong charge transfer is observed through the formation of a new HOMO state whose onset is located at 0.32 eV. The new HOMO state is formed by charge transfer from Na metal to the LUMO state of 6P; thus, the LUMO state is occupied and can be detected as the new HOMO state. Different from the 6P/Na interface, no similar shifts of peaks are observed at Na/6P interface, which is also related to the deposition mode of 6P. With the island deposition mode, the charge transfer between Na and molecules is stronger since Na atoms can diffuse into molecule layers deeply. In this way, the Fermi level is located at a higher stage; thus, the binding energies of all peaks are shown with higher values, and the band bending effect is not obviously detected in this case.

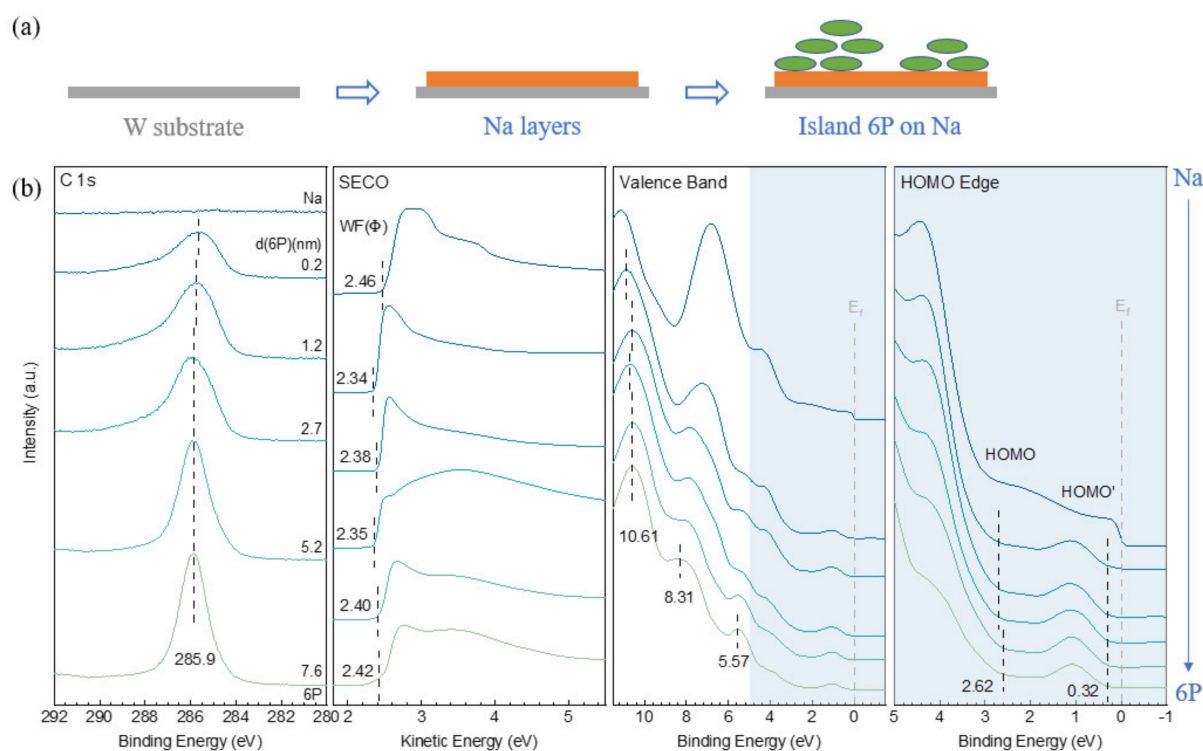


Figure 5. (a) Schematic of the 6P molecules and Na atoms deposition sequences. (b) XPS and UPS spectra of Na films with stepwise 6P deposition on a tungsten substrate.

3.3. DFT Calculation

The adsorption energies of optimized 6T-Na and 6T-Na₂ structures were calculated to further study the favourable sodiophilic sites of 6T molecules (Figure 6). The optimized structures of Na-adsorbed 6T are shown, and the adsorption energy is calculated as the energy difference between the optimized structure and the sum of a molecule and a Na atom. Three different optimized structures were calculated with one Na atom adsorbed on a 6T molecule. It is shown that the most favourable adsorption site is the central sulfur and the connected bridge carbon atoms. Anchored by the symmetric sulfur atoms, the Na atom is located at the centre and the adsorption energy is the largest one ($\Delta E_1 = -0.58$ eV). The neighbouring sulfur and the connected bridge carbon atoms are the second favourable sites, indicated by the slightly smaller adsorption energy ($\Delta E_2 = -0.56$ eV). In addition, Na can also be adsorbed by the sulfur atom, the connected carbon atom, and the aromatic carbon atom of the end group with a smaller adsorption energy ($\Delta E_3 = -0.47$ eV). Moreover, based on the most favourable sodiophilic site, the optimized structures of 6T with two adsorbed Na atoms were also calculated. As shown in Figure 6, the interaction sites are similar, and it is found that Na atoms can interact with both sides of 6T molecules simultaneously even at the same interaction site.

Our DFT results are in good agreement with the in-situ XPS results, which further supports our proposed mechanisms and provides a clearer understanding of the interaction process. When Na atoms are deposited on 6T layers, in the first step, they are anchored by two adjacent S_C atoms and interact with them and their bridge C_S atoms at the same time, generating the reduced S_{Na1} and C_S-Na species. Additionally, one S_C atom can be simultaneously reduced by two Na atoms at both sides, generating the more reduced S_{Na2} species. In the second step, Na atoms can diffuse into the standing 6T molecules and interact with both sides of molecules. Thus, the bridge C_S atoms are reduced by two Na atoms simultaneously, generating C_S-Na₂ species. When 6T molecules are deposited on Na films, the interaction can only happen at the interface, and the excess Na can interact with all sodiophilic sites of 6T including the aromatic C_C atoms of the end groups, generating the reduced C_C-Na species.

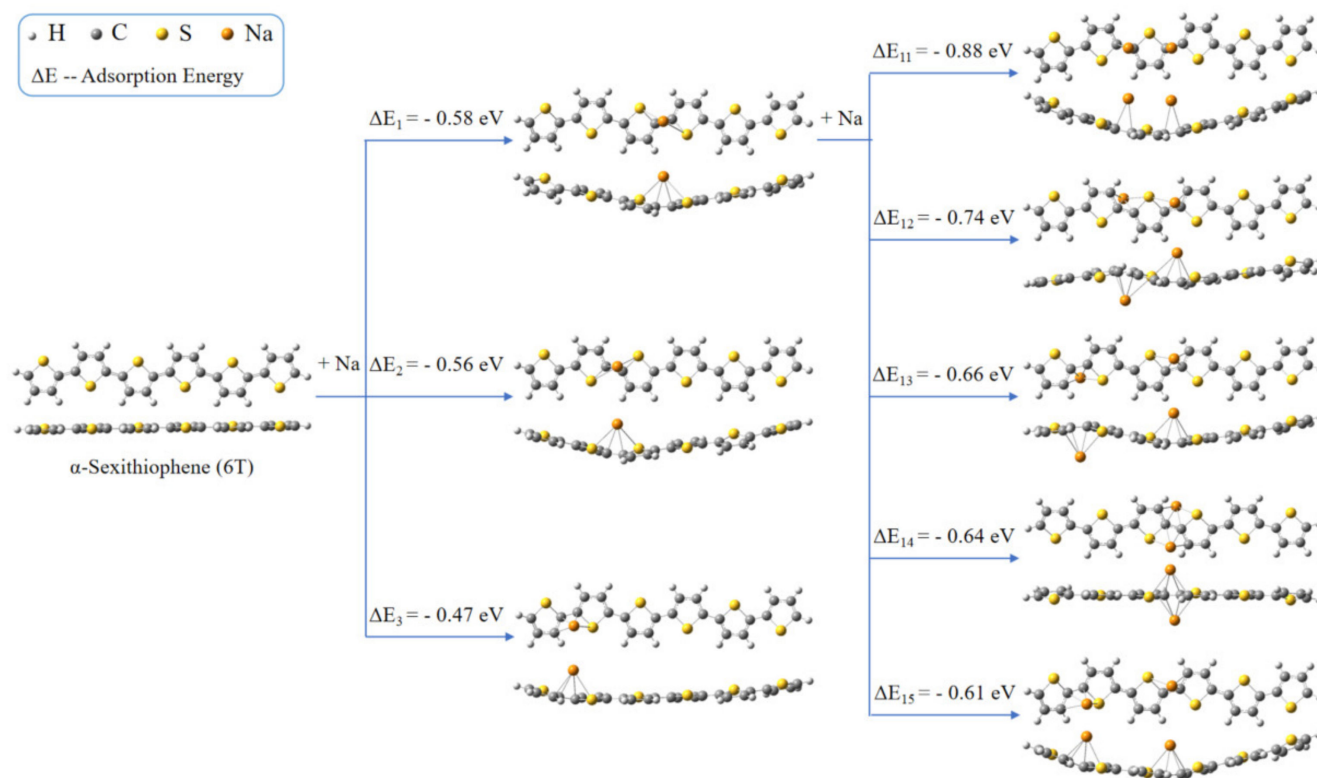


Figure 6. Calculated adsorption energy (ΔE) of optimized 6T-Na and 6T-Na₂ structures.

4. Conclusions

In this work, we studied the interaction process between Na metal and 6T/6P molecules via in-situ photoelectron spectroscopy investigations and DFT calculations. When Na atoms are deposited on 6T layers, they prefer to interact with the sulfur atoms and their connected carbon atoms, and they can diffuse into the standing 6T to interact at both sides of molecules. When the deposition sequence is reversed with 6T molecules deposited on Na films, the interaction can only happen at the interface, since the 6T molecules are lying down, and Na atoms cannot diffuse into molecules. For the interaction sites, besides the favourable sulfur and their connected carbon atoms, excess Na atoms can also interact with the aromatic carbon atoms of the end groups. In contrast, for the interaction between 6P and Na, no chemical reaction is observed, but strong charge transfer from Na metal to 6P molecules is detected, indicated by the band bending effect and formation of a LUMO-derived state. Our work reveals the sulfurization-induced sodiophilic sites with a model study of 6T/6P, which can draw a deeper understanding of the interaction between SMAs and protective materials, thus giving insights into the rational design of novel and advanced protective materials for the stabilization of SMAs. With these sodium-reactive sodiophilic sites, thiophene derivatives can be designed as electrolyte additives to increase the uniformity of composition distribution and stability of the as-formed SEI, facilitating uniform Na⁺ fluxes. In addition, they can also be designed as artificial protective layers of anodes, in which case, the uniform sodiophilic sites can homogenize Na⁺ fluxes, ensure uniform Na deposition and thus suppress the dendrite formation. For benzene derivatives, they are favorable for charge transfer; they can be used as the anode host materials to accommodate the deposited Na and guide the uniform sodium deposition with suppressed volume expansion.

Supplementary Materials: The following supporting information can be downloaded at: <https://www.mdpi.com/article/10.3390/batteries9010021/s1>, Figure S1: Na wettability tests of Cu, 6P-Cu, and 6T-Cu; Figure S2: UPS spectra for increasing 6T deposition on a silicon substrate; Figure S3: Thickness and surface morphology of (a) 6T and (b) 6P films characterized by AFM; Figure S4: XPS spectra of Na 1s in different experiments: Na on 6T, 6T on Na, Na on 6P, and 6P on Na; Table S1: Detailed peak fitting parameters in C 1s and S 2p XPS core-level spectra for 6T with increasing Na deposition; Table S2: Detailed peak fitting parameters in C 1s and S 2p XPS core-level spectra for Na with increasing 6T deposition.

Author Contributions: Y.L.: conceptualization, methodology, formal analysis, investigation, data curation, visualization, and writing—original draft preparation; X.L.: conceptualization, methodology, and formal analysis; C.J.: investigation; J.Y., Y.D. and Z.S.: writing—review and editing; W.C.: supervision, project administration and funding acquisition. All authors have read and agreed to the published version of the manuscript.

Funding: This research was funded by Singapore MOE grant under MOE2017-T2-2-052 and NUS R&G Postdoc Fellowship Program.

Institutional Review Board Statement: Not applicable.

Informed Consent Statement: Not applicable.

Data Availability Statement: Not applicable.

Conflicts of Interest: The authors declare no conflict of interest. The funders had no role in the design of the study; in the collection, analyses, or interpretation of data; in the writing of the manuscript; or in the decision to publish the results.

References

1. Wang, T.; Hua, Y.; Xu, Z.; Yu, J.S. Recent Advanced Development of Artificial Interphase Engineering for Stable Sodium Metal Anodes. *Small* **2022**, *18*, 2102250. [[CrossRef](#)] [[PubMed](#)]
2. Wang, H.; Matios, E.; Luo, J.; Li, W. Combining theories and experiments to understand the sodium nucleation behavior towards safe sodium metal batteries. *Chem. Soc. Rev.* **2020**, *49*, 3783–3805. [[CrossRef](#)] [[PubMed](#)]
3. Lee, J.; Kim, J.; Kim, S.; Jo, C.; Lee, J. A review on recent approaches for designing the SEI layer on sodium metal anodes. *Mater. Adv.* **2020**, *1*, 3143–3166. [[CrossRef](#)]
4. Zhao, C.; Lu, Y.; Yue, J.; Pan, D.; Qi, Y.; Hu, Y.-S.; Chen, L. Advanced Na metal anodes. *J. Energy Chem.* **2018**, *27*, 1584–1596. [[CrossRef](#)]
5. Li, Z.; Zhu, K.; Liu, P.; Jiao, L. 3D Confinement Strategy for Dendrite-Free Sodium Metal Batteries. *Adv. Energy Mater.* **2022**, *12*, 2100359. [[CrossRef](#)]
6. Chu, C.; Li, R.; Cai, F.; Bai, Z.; Wang, Y.; Xu, X.; Wang, N.; Yang, J.; Dou, S. Recent advanced skeletons in sodium metal anodes. *Energy Environ. Sci.* **2021**, *14*, 4318–4340. [[CrossRef](#)]
7. Cui, X.Y.; Wang, Y.J.; Wu, H.D.; Lin, X.D.; Tang, S.; Xu, P.; Liao, H.G.; Zheng, M.S.; Dong, Q.F. A Carbon Foam with Sodiophilic Surface for Highly Reversible, Ultra-Long Cycle Sodium Metal Anode. *Adv. Sci.* **2021**, *8*, 2003178. [[CrossRef](#)]
8. Sun, B.; Li, P.; Zhang, J.; Wang, D.; Munroe, P.; Wang, C.; Notten, P.H.; Wang, G. Dendrite-free sodium-metal anodes for high-energy sodium-metal batteries. *Adv. Mater.* **2018**, *30*, 1801334. [[CrossRef](#)]
9. He, X.; Jin, S.; Miao, L.; Cai, Y.; Hou, Y.; Li, H.; Zhang, K.; Yan, Z.; Chen, J. A 3D hydroxylated MXene/carbon nanotubes composite as a scaffold for dendrite-free sodium-metal electrodes. *Angew. Chem. Int. Ed.* **2020**, *59*, 16705–16711. [[CrossRef](#)]
10. Wang, H.; Matios, E.; Wang, C.; Luo, J.; Lu, X.; Hu, X.; Zhang, Y.; Li, W. Tin nanoparticles embedded in a carbon buffer layer as preferential nucleation sites for stable sodium metal anodes. *J. Mater. Chem. A* **2019**, *7*, 23747–23755. [[CrossRef](#)]
11. Li, Y.; Xu, P.; Mou, J.; Xue, S.; Huang, S.; Hu, J.; Dong, Q.; Yang, C.; Liu, M. Single Cobalt Atoms Decorated N-doped Carbon Polyhedron Enabled Dendrite-Free Sodium Metal Anode. *Small Methods* **2021**, *5*, 2100833. [[CrossRef](#)] [[PubMed](#)]
12. Xia, X.; Du, C.F.; Zhong, S.; Jiang, Y.; Yu, H.; Sun, W.; Pan, H.; Rui, X.; Yu, Y. Homogeneous Na Deposition Enabling High-Energy Na-Metal Batteries. *Adv. Funct. Mater.* **2022**, *32*, 2110280. [[CrossRef](#)]
13. Seh, Z.W.; Sun, J.; Sun, Y.; Cui, Y. A highly reversible room-temperature sodium metal anode. *ACS Cent. Sci.* **2015**, *1*, 449–455. [[CrossRef](#)] [[PubMed](#)]
14. Wang, S.; Chen, Y.; Jie, Y.; Lang, S.; Song, J.; Lei, Z.; Wang, S.; Ren, X.; Wang, D.; Li, X. Stable sodium metal batteries via manipulation of electrolyte solvation structure. *Small Methods* **2020**, *4*, 1900856.
15. Cao, R.; Mishra, K.; Li, X.; Qian, J.; Engelhard, M.H.; Bowden, M.E.; Han, K.S.; Mueller, K.T.; Henderson, W.A.; Zhang, J.-G. Enabling room temperature sodium metal batteries. *Nano Energy* **2016**, *30*, 825–830. [[CrossRef](#)]
16. Zheng, J.; Chen, S.; Zhao, W.; Song, J.; Engelhard, M.H.; Zhang, J.-G. Extremely stable sodium metal batteries enabled by localized high-concentration electrolytes. *ACS Energy Lett.* **2018**, *3*, 315–321. [[CrossRef](#)]

17. Sun, H.; Zhu, G.; Xu, X.; Liao, M.; Li, Y.-Y.; Angell, M.; Gu, M.; Zhu, Y.; Hung, W.H.; Li, J. A safe and non-flammable sodium metal battery based on an ionic liquid electrolyte. *Nat. Commun.* **2019**, *10*, 3302. [[CrossRef](#)]
18. Hu, X.; Matios, E.; Zhang, Y.; Wang, C.; Luo, J.; Li, W. Deeply cycled sodium metal anodes at low temperature and in lean electrolyte conditions. *Angew. Chem.* **2021**, *133*, 6043–6048. [[CrossRef](#)]
19. Wu, J.; Liu, J.; Lu, Z.; Lin, K.; Lyu, Y.-Q.; Li, B.; Ciucci, F.; Kim, J.-K. Non-flammable electrolyte for dendrite-free sodium-sulfur battery. *Energy Storage Mater.* **2019**, *23*, 8–16. [[CrossRef](#)]
20. Li, P.; Jiang, Z.; Huang, X.; Lu, X.; Xie, J.; Cheng, S. Nitrofullerene as an electrolyte-compatible additive for high-performance sodium metal batteries. *Nano Energy* **2021**, *89*, 106396. [[CrossRef](#)]
21. Shi, Q.; Zhong, Y.; Wu, M.; Wang, H.; Wang, H. High-performance sodium metal anodes enabled by a bifunctional potassium salt. *Angew. Chem.* **2018**, *130*, 9207–9210. [[CrossRef](#)]
22. Teng, W.; Wu, J.; Liang, Q.; Deng, J.; Xu, Y.; Liu, Q.; Wang, B.; Ma, T.; Nan, D.; Liu, J. Designing Advanced Liquid Electrolytes for Alkali Metal Batteries: Principles, Progress, and Perspectives. *Energy Environ. Mater.* **2022**. [[CrossRef](#)]
23. Bao, C.; Wang, B.; Liu, P.; Wu, H.; Zhou, Y.; Wang, D.; Liu, H.; Dou, S. Solid electrolyte interphases on sodium metal anodes. *Adv. Funct. Mater.* **2020**, *30*, 2004891. [[CrossRef](#)]
24. Hou, Z.; Wang, W.; Yu, Y.; Zhao, X.; Chen, Q.; Zhao, L.; Di, Q.; Ju, H.; Quan, Z. Poly (vinylidene difluoride) coating on Cu current collector for high-performance Na metal anode. *Energy Storage Mater.* **2020**, *24*, 588–593. [[CrossRef](#)]
25. Zhu, M.; Wang, G.; Liu, X.; Guo, B.; Xu, G.; Huang, Z.; Wu, M.; Liu, H.K.; Dou, S.X.; Wu, C. Dendrite-free sodium metal anodes enabled by a sodium benzenedithiolate-rich protection layer. *Angew. Chem.* **2020**, *132*, 6658–6662. [[CrossRef](#)]
26. Tian, H.; Shao, H.; Chen, Y.; Fang, X.; Xiong, P.; Sun, B.; Notten, P.H.; Wang, G. Ultra-stable sodium metal-iodine batteries enabled by an in-situ solid electrolyte interphase. *Nano Energy* **2019**, *57*, 692–702. [[CrossRef](#)]
27. Choudhury, S.; Wei, S.; Ozhabes, Y.; Gunceler, D.; Zachman, M.J.; Tu, Z.; Shin, J.H.; Nath, P.; Agrawal, A.; Kourkoutis, L.F. Designing solid-liquid interphases for sodium batteries. *Nat. Commun.* **2017**, *8*, 898. [[CrossRef](#)]
28. Shi, P.; Zhang, S.; Lu, G.; Wang, L.; Jiang, Y.; Liu, F.; Yao, Y.; Yang, H.; Ma, M.; Ye, S. Red Phosphorous-Derived Protective Layers with High Ionic Conductivity and Mechanical Strength on Dendrite-Free Sodium and Potassium Metal Anodes. *Adv. Energy Mater.* **2021**, *11*, 2003381. [[CrossRef](#)]
29. Zhao, Y.; Goncharova, L.V.; Lushington, A.; Sun, Q.; Yadegari, H.; Wang, B.; Xiao, W.; Li, R.; Sun, X. Superior stable and long life sodium metal anodes achieved by atomic layer deposition. *Adv. Mater.* **2017**, *29*, 1606663. [[CrossRef](#)]
30. Hou, Z.; Wang, W.; Chen, Q.; Yu, Y.; Zhao, X.; Tang, M.; Zheng, Y.; Quan, Z. Hybrid protective layer for stable sodium metal anodes at high utilization. *ACS Appl. Mater. Interfaces* **2019**, *11*, 37693–37700. [[CrossRef](#)]
31. Kim, Y.-J.; Lee, H.; Noh, H.; Lee, J.; Kim, S.; Ryou, M.-H.; Lee, Y.M.; Kim, H.-T. Enhancing the cycling stability of sodium metal electrodes by building an inorganic–organic composite protective layer. *ACS Appl. Mater. Interfaces* **2017**, *9*, 6000–6006. [[CrossRef](#)]
32. Wang, H.; Wang, C.; Matios, E.; Li, W. Facile stabilization of the sodium metal anode with additives: Unexpected key role of sodium polysulfide and adverse effect of sodium nitrate. *Angew. Chem.* **2018**, *130*, 7860–7863. [[CrossRef](#)]
33. Li, W.; Yao, H.; Yan, K.; Zheng, G.; Liang, Z.; Chiang, Y.-M.; Cui, Y. The synergetic effect of lithium polysulfide and lithium nitrate to prevent lithium dendrite growth. *Nat. Commun.* **2015**, *6*, 7436.
34. Wang, K.; Li, X.; Gao, J.; Sun, Q.; Yang, Z.; He, J.; Cui, S.; Huang, C. Self-Regulation Seaweed-Like Lithium Metal Anode Enables Stable Cycle Life of Lithium Battery. *Adv. Funct. Mater.* **2021**, *31*, 2009917. [[CrossRef](#)]
35. Yao, W.; Xu, M.; Qiu, W.; Wang, J.; Sun, Y.; Xu, J.; Zhang, Q. Ultralight PEDOT Functionalized Separators toward High-Performance Lithium Metal Anodes. *ChemElectroChem* **2021**, *8*, 2836–2845. [[CrossRef](#)]
36. Zheng, Y.; Fang, W.; Zheng, H.; Su, Y.; Liang, X.; Chen, C.; Xiang, H. A multifunctional thiophene-based electrolyte additive for lithium metal batteries using high-voltage LiCoO₂ cathode. *J. Electrochem. Soc.* **2019**, *166*, A3222. [[CrossRef](#)]
37. Li, T.; Wang, L.; Li, J. Carbon nanotube enables high-performance thiophene-containing organic anodes for lithium ion batteries. *Electrochim. Acta* **2022**, *408*, 139947.
38. Hou, C.-C.; Ma, C.; Zhang, S.-N.; Wang, L.-Y.; Wang, K.-X.; Chen, J.-S. Polymeric Schiff Base with Thiophene Rings for Sodium-Ion Batteries. *ACS Appl. Energy Mater.* **2022**, *5*, 13802–13807. [[CrossRef](#)]
39. Liu, Y.; Lian, X.; Xie, Z.; Yang, J.; Ding, Y.; Chen, W. Probing fluorination promoted sodiophilic sites with model systems of F16CuPc and CuPc. *Front. Optoelectron.* **2022**, *15*, 19.
40. Powell, C. The quest for universal curves to describe the surface sensitivity of electron spectroscopies. *J. Electron. Spectrosc. Relat. Phenom.* **1988**, *47*, 197–214.
41. Frisch, M.J.; Trucks, G.W.; Schlegel, H.B.; Scuseria, G.E.; Robb, M.A.; Cheeseman, J.R.; Scalmani, G.; Barone, V.; Petersson, G.A.; Nakatsuji, H.; et al. *Gaussian 16*, revision B.01; Gaussian Inc.: Wallingford, CT, USA, 2016.
42. Stephens, P.J.; Devlin, F.J.; Chabalowski, C.F.; Frisch, M.J. Ab initio calculation of vibrational absorption and circular dichroism spectra using density functional force fields. *J. Phys. Chem.* **1994**, *98*, 11623–11627. [[CrossRef](#)]
43. Ivanko, J.; Haber, T.; Resel, R.; Netzer, F.P.; Ramsey, M.G. Electronic and geometric structure of electro-optically active organic films and associated interfaces. *Thin Solid Film.* **2006**, *514*, 156–164. [[CrossRef](#)]
44. Toyoshima, H.; Inoue, K.; Hiraga, K.; Ohno, S.; Tanaka, M. Determination of molecular orientation of α -sexithiophene on passivated Si (001) by means of optical reflectance spectroscopic methods. *Surf. Sci.* **2013**, *616*, 36–43. [[CrossRef](#)]
45. Chen, L.; Li, H.; Wee, A.T.S. One-dimensional molecular chains with dispersive electronic states. *Nano Lett.* **2009**, *9*, 4292–4296. [[CrossRef](#)] [[PubMed](#)]

46. Duhm, S.; Heimel, G.; Salzmann, I.; Glowatzki, H.; Johnson, R.L.; Vollmer, A.; Rabe, J.P.; Koch, N. Orientation-dependent ionization energies and interface dipoles in ordered molecular assemblies. *Nat. Mater.* **2008**, *7*, 326–332. [[CrossRef](#)]
47. Wagner, T.; Fritz, D.R.; Zeppenfeld, P. α -6T on Ag(110): The formation of the wetting layer. *Synth. Met.* **2011**, *161*, 2006–2010. [[CrossRef](#)]
48. Glowatzki, H.; Duhm, S.; Braun, K.F.; Rabe, J.P.; Koch, N. Molecular chains and carpets of sexithiophenes on Au(111). *Phys. Rev. B* **2007**, *76*, 125425. [[CrossRef](#)]
49. Grobosch, M.; Knupfer, M. Electronic properties of the interface between the organic semiconductor α -sexithiophene and polycrystalline palladium. *Org. Electron.* **2008**, *9*, 767–774. [[CrossRef](#)]
50. Schwieger, T.; Liu, X.; Peisert, H.; Adolphi, B.; Kiriya, N.; Knupfer, M. Electronic properties of interfaces between different sexithiophenes and gold. *J. Appl. Phys.* **2005**, *97*, 123712. [[CrossRef](#)]
51. Grobosch, M.; Knupfer, M. Energy level alignment and interface states at α -sexithiophene/Ag interfaces. *Org. Electron.* **2007**, *8*, 625–630. [[CrossRef](#)]
52. Blumstengel, S.; Koch, N.; Sadofev, S.; Schäfer, P.; Glowatzki, H.; Johnson, R.L.; Rabe, J.P.; Henneberger, F. Interface formation and electronic structure of α -sexithiophene on ZnO. *Appl. Phys. Lett.* **2008**, *92*, 193303. [[CrossRef](#)]
53. Endres, J.; Pelczar, I.; Rand, B.P.; Kahn, A. Determination of Energy Level Alignment within an Energy Cascade Organic Solar Cell. *Chem. Mater.* **2016**, *28*, 794–801. [[CrossRef](#)]
54. Ivanco, J.; Netzer, F.P.; Ramsey, M.G. Dissociation of sexithiophene on Al(111) surface. *Org. Electron.* **2007**, *8*, 545–551. [[CrossRef](#)]
55. Koch, N.; Chan, C.; Kahn, A.; Schwartz, J. Lack of thermodynamic equilibrium in conjugated organic molecular thin films. *Phys. Rev. B* **2003**, *67*, 195330. [[CrossRef](#)]
56. Koch, N.; Yu, L.M.; Parenté, V.; Lazzaroni, R.; Johnson, R.L.; Leising, G.; Pireaux, J.J.; Brédas, J.L. Evidence for physisorption of aluminum on the surface of electroluminescent sexiphenyl. *Adv. Mater.* **1998**, *10*, 1038–1043. [[CrossRef](#)]
57. Schroeder, P.G.; France, C.B.; Parkinson, B.A.; Schlaf, R. Orbital alignment at p-sexiphenyl and coronene/layered materials interfaces measured with photoemission spectroscopy. *J. Appl. Phys.* **2002**, *91*, 9095–9107. [[CrossRef](#)]
58. Zhang, Z.; Yates, J.T., Jr. Band bending in semiconductors: Chemical and physical consequences at surfaces and interfaces. *Chem. Rev.* **2012**, *112*, 5520–5551. [[CrossRef](#)]
59. Koch, N.; Jäckel, F.; Ghijssen, J.; Rojas, M.C.; Grioni, M.; Rabe, J.P.; Johnson, R.L.; Kahn, A.; Pireaux, J.J. Observation of filled states at the Fermi-level in alkali-metal intercalated organic films: Dependence on substrate work function. *J. Electron. Spectrosc. Relat. Phenom.* **2005**, *144–147*, 495–498. [[CrossRef](#)]
60. Koch, N.; Rajagopal, A.; Ghijssen, J.; Johnson, R.; Leising, G.; Pireaux, J.-J. Bipolaron: The stable charged species in n-doped p-sexiphenyl. *J. Phys. Chem. B* **2000**, *104*, 1434–1438. [[CrossRef](#)]
61. Andreev, A. Morphology and growth kinetics of organic thin films deposited by hot wall epitaxy. *Org. Electron.* **2004**, *5*, 23–27. [[CrossRef](#)]
62. Teichert, C.; Hlawacek, G.; Andreev, A.Y.; Sitter, H.; Frank, P.; Winkler, A.; Sariciftci, N.S. Spontaneous rearrangement of para-sexiphenyl crystallites into nano-fibers. *Appl. Phys. A* **2005**, *82*, 665–669. [[CrossRef](#)]

Disclaimer/Publisher’s Note: The statements, opinions and data contained in all publications are solely those of the individual author(s) and contributor(s) and not of MDPI and/or the editor(s). MDPI and/or the editor(s) disclaim responsibility for any injury to people or property resulting from any ideas, methods, instructions or products referred to in the content.